Materials Today Bio 34 (2025) 102219

Contents lists available at ScienceDirect

Materials Today Bio

journal homepage: www.journals.elsevier.com/materials-today-bio

Dual-responsive copper complex delivered by dissolvable microneedle promotes polymicrobial infection eradication and cutaneous wound healing

Sumanta Ghosh [a,1], Soumen Ghosh [b,1], Kelvin W.K. Yeung [d], Chenjie Xu [f], Jun Wu [e], Congyang Mao [d], Zemin Ling [g], Kou Okuro [b,c], Wei Qiao [a,e,*]

[a] Applied Oral Sciences and Community Dental Cares, Faculty of Dentistry, The University of Hong Kong, Hong Kong Special Administrative Region of China
[b] Department of Chemistry, The University of Hong Kong, Hong Kong Special Administrative Region of China
[c] State Key Laboratory of Synthetic Chemistry, The University of Hong Kong, Hong Kong Special Administrative Region of China
[d] Department of Orthopaedics and Traumatology, Faculty of Medicine, The University of Hong Kong, Hong Kong Special Administrative Region of China
[e] Shenzhen Key Laboratory for Innovative Technology in Orthopaedic Trauma, the University of Hong Kong-Shenzhen Hospital, Shenzhen, 518053, China
[f] Department of Biomedical Engineering, City University of Hong Kong, Tat Che Avenue, Hong Kong Special Administrative Region of China
[g] Shenzhen Key Laboratory of Bone Tissue Repair and Translational Research, Department of Orthopaedic Surgery, The Seventh Affiliated Hospital, Sun Yat-sen University, Shenzhen, China

ARTICLE INFO

Keywords:
Polymicrobial infection
Immunomodulation
Copper
Microneedle
Wound healing

ABSTRACT

Cross-kingdom polymicrobial wound infections present significant clinical challenges, including persistent pathogen colonization, delayed healing, and an elevated risk of complications. Despite the broad-spectrum antimicrobial activity and immunomodulatory properties of copper ions (Cu^{2+}), their therapeutic efficacy in infectious wound management is often suboptimal due to the lack of precise control of ion release kinetics. Here, we developed a dissolvable microneedle dressing loaded with our novel copper complex containing an Azo-Schiff base (Cu-Azo@DMN). This system demonstrates oxidative stress-mediated antimicrobial activity and enables pH-responsive Cu^{2+} release in the acidic polymicrobial infection microenvironment. Furthermore, Cu-Azo@DMN also exhibits enhanced antimicrobial efficacy through photo-responsive Cu^{2+} release. Following pathogen clearance, the system autonomously tunes down Cu^{2+} release to resolve inflammation and promote angiogenesis, thereby facilitating tissue regeneration. Collectively, our findings feature Cu-Azo@DMN as a smart wound dressing that enables dual-responsive Cu^{2+} release, offering a streamlined management of cross-kingdom polymicrobial infections and immunomodulation wound healing.

1. Introduction

Wound infection poses a significant threat to tissue integrity and is commonly caused by multiple microbial species rather than a single microorganism [1,2]. More than 80 % of common skin and soft tissue infections are polymicrobial, involving cross-kingdom species [3]. The biofilm development in the infected wound bed further exacerbates the severity by providing a protective layer for the pathogens. Additionally, the interspecies interactions among cross-kingdom microbial species within the biofilm also lead to antibiotic resistance [2,4]. For instance, wounds infected with bacteria, such as *S. aureus*, *P. aeruginosa*, and *Streptococcus* spp., often interact with fungal species like *C. albicans* [5,6]. In the presence of *C. albicans*, *S. aureus* forms a persister biofilm and becomes more resistant to traditional antibiotics [6]. It was reported that *C. albicans*-secreted β-1,3-glucan cell wall component rapidly coated *S. aureus* surface in the biofilm niche and significantly reduced the antibiotic penetration [7]. Additionally, the hyphal form of C. albicans within the biofilm is more resistant to macrophage phagocytosis as it can evade macrophage-mediated clearance through pore-forming proteins, leading to increased pathogenic severity [8]. Nevertheless, conventional antimicrobial strategies primarily target single causative pathogens, and the interactions among multiple microbial species concerning pathogenicity and antibiotic responsiveness are poorly investigated. Therefore, future therapeutic approaches need

This article is part of a special issue entitled: Multiscale Composites published in Materials Today Bio.

* Corresponding author. Applied Oral Sciences and Community Dental Cares Faculty of Dentistry, The University of Hong Kong, Hong Kong Special Administrative Region of China.
E-mail address: drqiao@hku.hk (W. Qiao).

[1] These authors contributed equally.

https://doi.org/10.1016/j.mtbio.2025.102219
Received 23 April 2025; Received in revised form 17 August 2025; Accepted 19 August 2025
Available online 21 August 2025

to be designed to eliminate polymicrobial cross-kingdom infection with minimal adverse effects [9].

Over the years, various classes of antimicrobial agents, including conventional antibiotics, antimicrobial peptides and organometallic compounds, have been developed to address the challenge of infected wound healing [4,10]. Among these, divalent metal cations such as silver (Ag^{2+}), copper (Cu^{2+}), zinc (Zn^{2+}), and manganese (Mn^{2+}) have gained significant attention due to their excellent biocompatibility, potent antimicrobial effects, and reduced microbial resistance development [4,11,12]. However, the clinical translation of them is still impeded by many shortcomings. For instance, Ag^{2+} can cause toxicity and hyperpigmentation [13]. Similarly, Zn^{2+} and Mn^{2} lead to unwanted tissue accumulation and disrupt normal cell metabolism [14,15]. Among them, Cu^{2+} showed broad-spectrum antimicrobial effects against diverse pathogens [4,16]. A recent clinical study showed that the copper dressing contributed to ~2.4 times higher wound area reduction than a conventional silver-based dressing [17].

Despite the promising efficacy of copper-based therapeutics, there are several limitations which should be overcome for their safe clinical application [4,16,18]. For instance, constant maintenance of Cu^{2+} concentration at an optimal level at the infection site, overcoming the body fluid flow, is challenging [19,20]. Nonetheless, Cu^{2+} predominantly exhibits antimicrobial and immunomodulatory activity in a dose-dependent manner [21,22]. Moreover, optimal Cu^{2+} concentrations exhibit various physiological roles at multiple stages of infectious wound healing, from pathogen eradication to tissue regeneration [16]. Therefore, it is imperative to develop a controlled Cu^{2+} delivery strategy tailored to the dynamic needs of infectious wound healing. Recently, several Cu-based metal complexes, metal-organic frameworks, and smart hydrogels have been reported to control Cu^{2+} by specific endogenous or exogenous stimuli [18,23]. For instance, pH-responsive Cu^{2+}-releasing hydrogel exhibited tailored antibacterial action in an acidic wound environment [24]. Interestingly, exogenous stimuli like light or magnetism have been utilised for more precise control over Cu^{2+} release [25]. Nonetheless, different types of skin wounds exhibit varying local pH levels, and it is influenced by several individual factors, including the patient's age, wound location, medication use, and physiological variations [26,27]. For instance, hospital-acquired wound infections often show an acidic pH, whereas second-degree burns tend to have an elevated pH [27]. Given these variations, the dual-responsive therapeutics triggered by both external light and internal pH offer a versatile solution for managing diverse wound conditions. Furthermore, the pH of the wound microenvironment changes over time as healing progresses. Therefore, the responsiveness to multiple stimuli ensures more flexibility in the adjustment of Cu^{2} delivery, ensuring its effectiveness in infectious wound management [27]. However, a controlled Cu-delivery platform capable of managing cross-kingdom polymicrobial infections and immunomodulatory wound healing in response to both internal and external stimuli is currently limited.

Herein, a dual-responsive Cu(II) complex containing biphenyl-based Azo-Schiff base (Cu-Azo) was synthesized, which exhibited on-demand release of Cu^{2+} upon internal (pH) and external (light) stimulus. The presence of amide (-CONH-) and Schiff base (-C=N-) linkages enabled pH-responsive cleavage in the acidic infection environment, while the light-sensitive azo (-N=N-) moieties exhibited photo-degradation under external light stimulation (Scheme 1A). This dual responsiveness enabled precise control over Cu^{2+}-release at different stages of infection healing. Initially, dissolvable microneedles loaded with Cu-Azo (Cu-Azo@DMN) contribute to burst Cu^{2+} release to exhibit potent antimicrobial activity against polymicrobial infection. Further external light exposure enables higher antimicrobial potency by enhancing rapid Cu^{2+} release. After the infection eradication, Cu-Azo@DMN spontaneously resolved inflammation and promoted tissue regeneration (Scheme 1B). Taken together, dual-responsive Cu-Azo holds great promise for treating polymicrobial-infected cutaneous wounds.

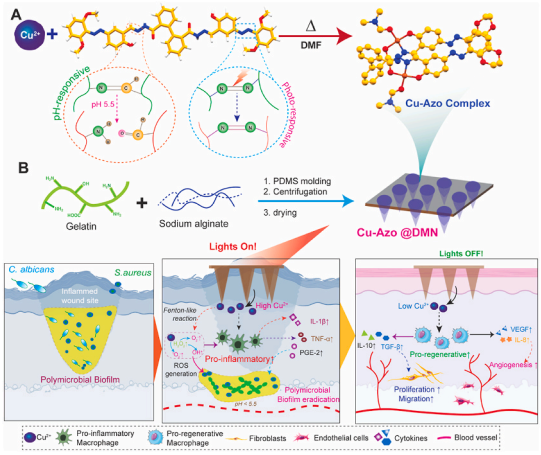

Scheme 1. Schematic illustration of (**A**) design and synthesis of dual-responsive (pH and light) Cu-Azo complex and (**B**) working principle of dissolvable microneedles loaded with Cu-Azo complex (Cu-Azo@DMN) for the treatment of infectious cutaneous wounds. Polymicrobial infections comprising bacteria and fungi species form complex biofilms that impair the cutaneous wound healing process. The Cu-Azo complex dissociates in response to the acidic biofilm microenvironment and external light stimulation for effective clearance of pathogens. Following the infection eradication, the Cu-Azo complex reduced Cu^{2+} release to shift its action towards inflammation resolution and tissue regeneration, thereby accomplishing infectious wound healing.

2. Results and discussion

2.1. Synthesis and characterization of Cu-Azo complex

To synthesize the dual-responsive Cu-Azo complex, we have followed three consecutive chemical reactions for the introduction of azo (N=N) moiety and Schiff linkage within the ligand framework. At first, 5-((2,6-dimethoxyphenyl) diazenyl)-2-hydroxybenzaldehyde was synthesized by a diazotization reaction between salisaldehyde and 2,6-dimethoxy aniline (Scheme S1, Fig. S1). Then, the ligand H_2L was synthesized by the reaction between diphenic acid-hydrazide and 5-((2,6-dimethoxy phenyl) diazenyl)-2-hydroxybenzaldehyde (Scheme S2, Fig. S2). Finally, the linker H_2L was treated with copper chloride in methanol under reflux conditions to form the Cu-Azo complex, which was then crystallized in a DMF/ether medium (Scheme 1A, Fig. S3). The Cu-Azo complex, with the stoichiometry $Cu_2(L_2)(DMF)_2$, was a neutral species that exhibited a monoclinic single crystal lattice with space group $C_{2/c}$. The asymmetric unit of the Cu-Azo crystal contained two independent Cu^{2+}, each positioned within one arm of the biphenyl moiety (Fig. 1A). Each Cu(II) centre displayed square planar coordination binding with two oxygen atoms, one nitrogen atom from the ligand, and one oxygen atom from a DMF molecule (Fig. 1B and C). Furthermore, Scanning Electron Microscopy (SEM) and Energy Dispersive X-ray (EDX) analysis showed the uniform distribution of the Cu in the amorphous powder of the Cu-Azo complex (Fig. 1E). The mass spectrometric analysis revealed the molecular weight of the Cu-Azo complex of about 1074.215 (m/z^+ = 1075.21, Fig. S3). The Oak Ridge Thermal-Ellipsoid Plot (ORTEP) of Cu-Azo with 50 % atomic probability is depicted in Fig. S4.

The crystallographic analysis revealed that upon complexation with Cu^{2+}, the dihedral angle between the two phenyl rings of the biphenyl unit was reduced to 59.71°, indicating substantial twisting compared to the free ligand, where two arms of the biphenyl moiety contained Cu^{2+} in square planar conformation (Fig. 1B). The diffraction parameters were listed in Table S1. The crystal packing showed that clustered water molecules connected the molecular units through H-bonding interactions (Fig. 1C). Clustered water molecules connect three units by O-H, N-H, and C-H-O interactions. Concurrently, π-π stacking and C-H-π

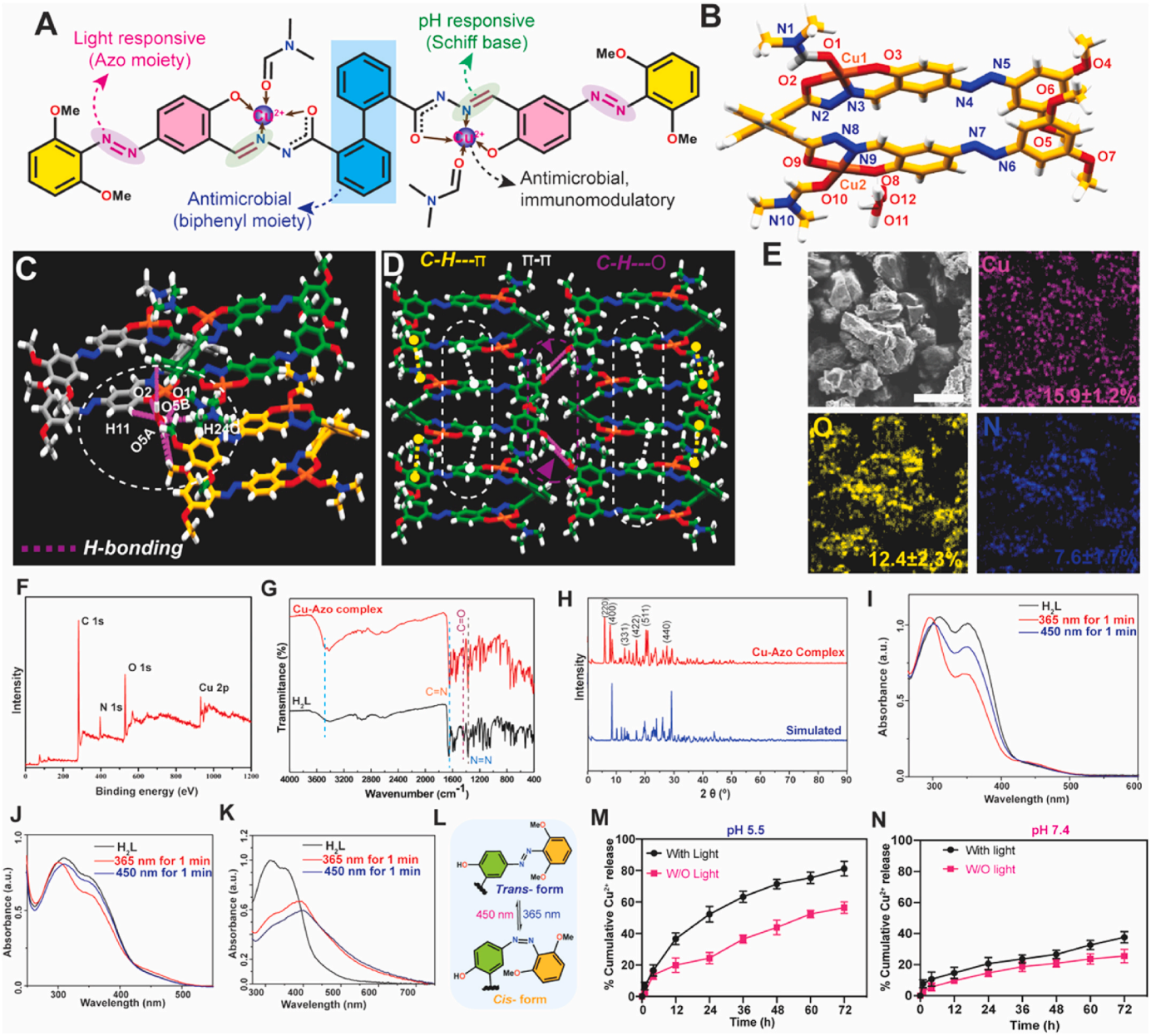

Fig. 1. Synthesis and characterization of Cu-Azo coordination complex. (**A**) Molecular structure of the Cu-Azo complex; the dotted arrows indicate different characteristics of various groups present in the complex. (**B**) Crystal structure of Cu-Azo complex; (**C**) Hydrogen bonding interactions within crystal lattice; (**D**) π-π stacking and C-H–π interactions within crystal lattice; (**E**) Representative SEM and EDX mapping of Cu-Azo complex indicating the presence of Cu, (scale = 50 μm). (**F**) XPS survey spectra of Cu-Azo complex, (**G**) FTIR spectra of H_2L and Cu-Azo complex, and (**H**) PXRD spectra of Cu-Azo complex and simulated spectra obtained from the single crystal XRD data. Photoswitching behaviour of Cu-Azo Complex. Photoisomerization of H_2L ligand in (**I**) Chloroform, (**J**) PBS buffer at pH 7.4, and (**K**) PBS buffer at pH 5.5. (**L**) Schematic representation of the photoswitching phenomenon of the Cu-Azo complex. Difference in release profile of Cu^{2+} from Cu-Azo complex at (**M**) pH 5.5 and (**N**) pH 7.4 with (W/) and without (W/O) exposure to light. The data demonstrated >50 % of the Cu^{2+} was released within 48 h under acidic pH-5.5, and further light stimulation resulted in ~80 % Cu^{2+} release. Data were presented as mean ± SD.

interactions facilitated stable crystal lattice formation (Fig. 1D).

To confirm the oxidation state of Cu in the Cu-Azo complex, X-ray photoelectron spectroscopy (XPS) was employed (Fig. 1F–S5). The presence of peaks with binding energies (B.E.) at 932.36 and 934.62 eV corresponded to Cu 2p3/2, while the peaks at 951.95 and 954.41 eV corresponded to Cu 2p1/2. These, along with ΔB.E. of 19.59 and 19.79 eV and the three satellite peaks at 941.84, 944.36, and 962.65 eV, confirmed the Cu(II) oxidation state. Two deconvoluted peaks at 530 and 534 eV in the O1s spectrum suggested phenolic OH and amide C-O of H_2L, respectively (Fig. S5). This indicated that the charge transfer from O to Cu resulted in higher binding energy. The Cu-Azo were further characterized by FTIR spectroscopy (Fig. 1G), confirming the presence of C=O, C=N, and N=N bonds at 1663.92, 1649.71, and 1542 cm^{-1}, respectively [28]. Powder X-ray diffraction (PXRD) spectra (Fig. 1H) also showed peaks at 2θ = 9.5°, 13.5°, 17.5°, and 19.1° and verified a square planner crystal lattice of Cu-Azo.

2.2. Dual-responsiveness of Cu-Azo complex

The photoisomerization properties of the H_2L ligand and Cu-Azo complex were studied by UV–visible and NMR spectroscopy (Fig. 1I & S6). The UV spectra of H_2L in chloroform depicted broad absorption bands at 310 and 350 nm corresponding to π−π* transitions and moderate absorbance bands at 450 nm corresponding to n−π* transitions

(Fig. 1J). Irradiation of H_2L with 365 nm light caused blue shifting in the absorption spectrum due to cis isomer formation with intensity reduction in the π−π* band (Fig. 1K). The n−π* bands underwent a hyperchromic shift with no distinct wavelength change (Table S1). Isomerization from cis to trans was achieved by irradiating with 450 nm. ^{1}H NMR experiment in $CDCl_3$ also indicated isomerization of the trans-to-cis form of H_2L upon irradiation of 365 nm light, as evidenced by the chemical shift changes of the protons in the azobenzene part (Fig. S6). The photo-isomerism of H_2L was tested in an aqueous buffer (pH 7.4), which also reconfirmed similar observations. However, at pH 5.5 after 365 nm light exposure, H_2L showed a substantial hypochromic shift in the absorption intensity, along with a new band which was irreversible even after irradiation by 450 nm light (Fig. 1K and L). Notably, the spectra didn't show any significant changes at pH 5.5 without light irradiation, indicating that 365 nm light irradiation led to photocleaving of the azo linkages and complex dissociation. Although many photo-switchable molecules have been reported previously, light-responsive metal complexes remain relatively rare. This is mainly due to restrictions of the metal ion coordination centre, which hinders geometric alterations during photo-switching [29–31].

The UV–visible spectra of the Cu-Azo complex in DMSO displayed broad absorption bands at 340 nm corresponding to a π−π* transition at 397 nm, indicating ligand-to-metal charge transfer (Fig. S7A). The weak n−π* absorption for Azo might get shadowed under broadband at 400 nm. The 365 nm light irradiation on the Cu-Azo complex induced a slight hypochromic shift in its absorption profiles, indicating cis isomer formation [29,32]. However, changes in n−π* bands had not been observed [33]. To investigate the photo-sensitivity, the complex was exposed to 450 nm light, and no significant change in the spectra was observed, indicating the structural rigidity of the complex [29,32]. Furthermore, the cis-trans photo-isomerism of the Cu-Azo complex was also tested at pH 7.4 and 5.5 (Fig. S7A–C). An irreversible decrease in absorbance within the 300 nm–400 nm range was evident at pH 5.5 upon light exposure (Fig. S7C). Collectively, these results indicated that Cu-Azo complex exhibits photodecomposition under an acidic environment and simultaneous light stimulation. Moreover, in the Cu-Azo complex, the azo linkage predominantly exists in the trans-form. Upon irradiation with 365 nm light, the bond attempts to isomerize to the cis form; however, the rigidity imposed by complex formation restricts this rotation. This restriction leads to gradual degradation of the complex upon prolonged UV exposure, resulting in the release of Cu^{2+}.

The dual-responsive Cu^{2+} release from the Cu-Azo complex was determined using inductively coupled plasma-optical emission spectrometry (ICP-OES). As shown in Fig. 1M, >50 % of the Cu^{2+} was released within 48 h under acidic pH-5.5, and further light stimulation resulted in ~80 % Cu^{2+} release. In contrast, at pH-7.4 (Fig. 1N), the Cu^{2+} released from the Cu-Azo complex remained constrained, regardless of light stimulation. The presence of Schiff base (-CH=N-) linkages

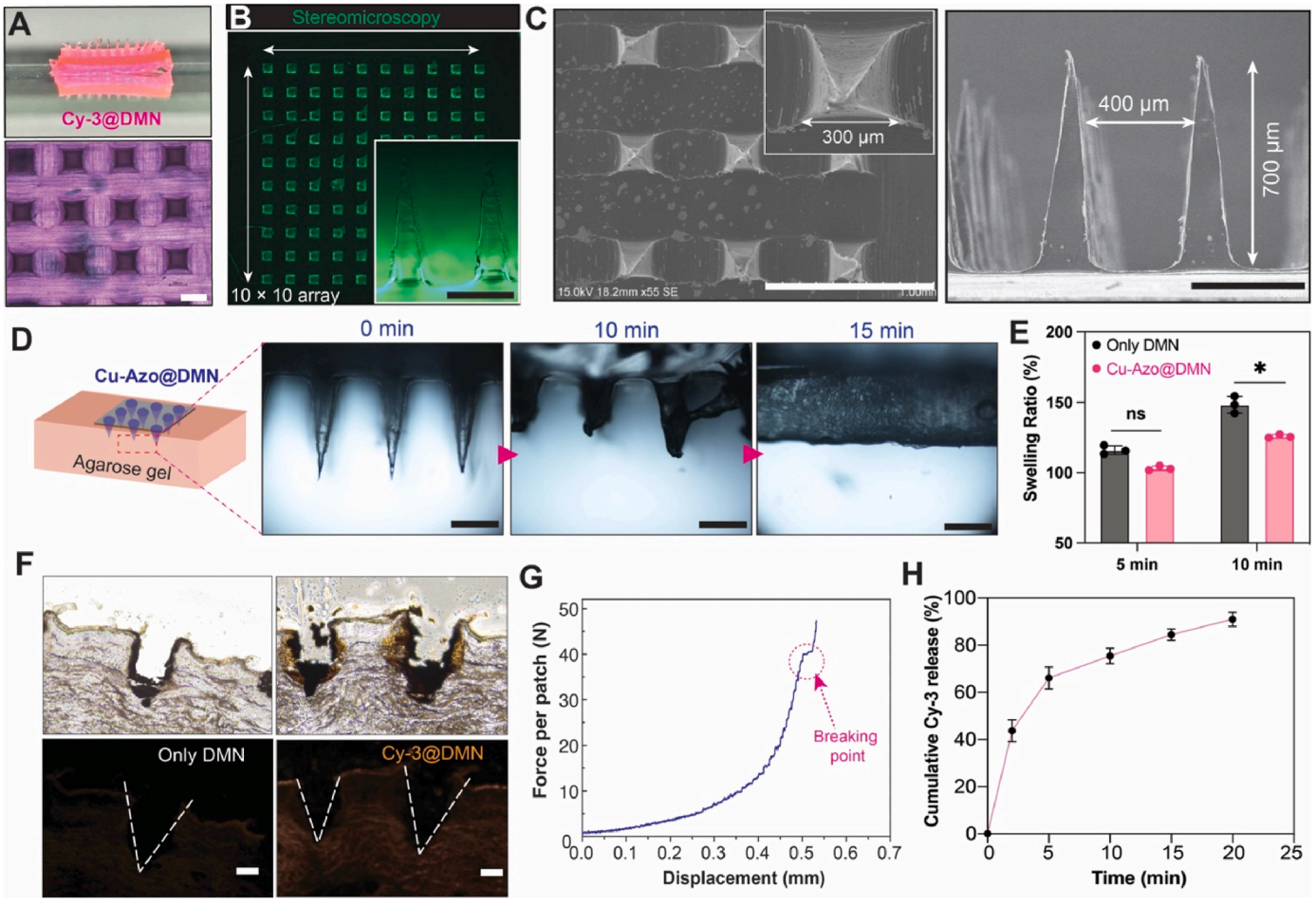

Fig. 2. Fabrication and characterization of Cu-Azo@DMN. (**A**) Optical images of Cy3-loaded DMN (i.e., Cy3@DMN). (**B**) Representative stereomicroscope images of a 10 × 10 array of Cy3@DMNs, scale bar = 500 μm. (**C**) Representative SEM images of DMN indicating the dimension of each needle, scale bar = 1 mm (left), 500 μm (right). (**D**) Representative optical images showing the dissolution of Cu-Azo@DMN inside an agarose gel, scale bar = 250 μm. (**E**) Quantification of water swellability of Cu-Azo@DMN, (n = 3). (**F**) Representative microscopic images of porcine skin after Cy-3@DMNs application, scale bar = 50 μm. (**G**) Force vs. displacement curve obtained from the compression test of Cu-Azo@DMN. (**H**) Cy3 release profile from the Cu-Azo@DMN in PBS. Data were presented as mean ± SD. *$p < 0.05$.

enables the Cu-Azo complex to be pH-responsive, as these bonds cleave under acidic conditions due to the protonation of N-atoms and result in amine and carbonyl components. When the -CH=N- linkage breaks, the complex begins to degrade, releasing Cu^{2+}. Overall, these findings demonstrated that Cu-Azo complex can exhibit controlled release of Cu^{2+} ions which is required for the infection control (early phase) and tissue repair (later phase).

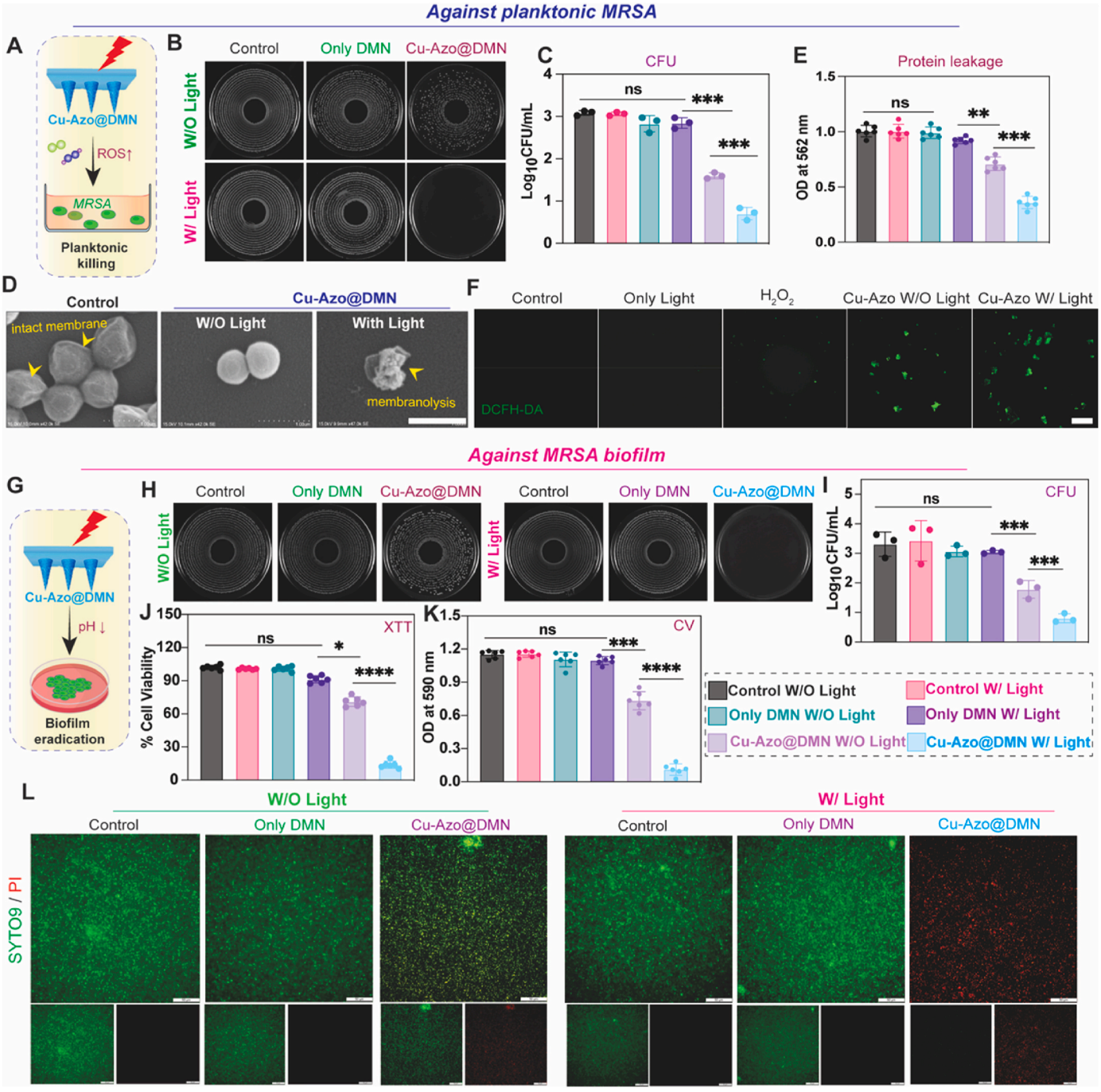

Fig. 3. The antibacterial activity of Cu-Azo@DMN against planktonic MRSA. (**A**) Schematic illustration of the planktonic antimicrobial activity of Cu-Azo@DMN. Representative optical images (**B**) and corresponding statistical comparison (**C**) of CFU for planktonic MRSA after 24 h of Cu-Azo@DMN treatment (n = 3). (**E**) Representative SEM images showing light-triggered Cu-Azo complex led to the damage of the cell wall of MRSA, scale bar = 1 μm. (**E**) Detection of protein leakage from MRSA after different treatments by BCA assay. (**F**) Representative fluorescence images of DCFH-DA indicating ROS generation from the MRSA, scale bar = 10 μm. (**G**) Schematic of experiment assessing the antibiofilm activity of Cu-Azo@DMN. Representative optical images (**H**) and corresponding statistical comparison (**I**) of CFU for MRSA biofilm after different treatments (n = 3). (**J**) Quantifications of the XTT assay for assessing cell viability in MRSA biofilm after different treatments. (**K**) Quantitative analysis of crystal violet (CV) staining at OD 590 nm for determining biofilm biomass (n = 6). (**L**) Representative confocal microscopic images for live/dead assay of MRSA biofilm after different treatments, scale = 50 μm, (n = 3). The index images below indicate the individual channels. Data were presented as mean ± SD. $^{*}p < 0.05$, $^{**}p < 0.01$, $^{***}p < 0.001$. (For interpretation of the references to colour in this figure legend, the reader is referred to the Web version of this article.)

2.3. Fabrication and characterizations of Cu-Azo@DMN

To achieve local transdermal delivery of the Cu-Azo complex, we loaded the Cu-Azo complex into dissolvable microneedles (DMN) (Fig. 2A and B). The DMN patch, composed of gelatin and sodium alginate, was fabricated using a polydimethylsiloxane (PDMS)-based micro-molding process. Subsequently, FTIR spectra and EDX analysis confirmed the successful incorporation of the Cu-Azo complex within the microneedle (Figs. S8 and S9). SEM images demonstrated pyramidal-shaped microneedles with a length and width of 700 μm and 300 μm, respectively (Fig. 2C). Furthermore, we examined the water swellability of the Cu-Azo@DMN by inserting it into 2 % agarose gel, mimicking native human skin and observed complete dissolution of the Cu-Azo@DMN within 15 min (Fig. 2D). Additionally, the swelling ratio of the Cu-Azo@DMN was slightly decreased compared with DMN, which might be attributed to the limited diffusion of water molecules into the dense Cu-Azo complex encapsulated polymer matrix (Fig. 2E) [34,35]. Notably, the DMN is quite suitable for wound infection, due to its rapid release (within 10–15 min) capability and disrupting the preformed biofilm to enhance the Cu-Azo penetration inside the deep biofilm niche [36], also minimizing hazardous sharp wastes, injuries, and transmission of blood-borne pathogens [37].

The delivery efficacy and skin penetration ability were assessed by inserting the fluorescently labelled Cy3@DMN into a porcine skin ex vivo model (Fig. 2F). The precise disruption of the stratum corneum layer to a depth of approximately 300 μm confirmed the penetration of microneedles into the skin tissue, thereby increasing drug concentration at the site of infection compared to conventional topical formulations such as creams, ointments, and lotions [38]. Additionally, fluorescence images demonstrated adequate diffusion of Cy3 within the subcutaneous tissue after the dissolution of the DMN [39]. The Cu-Azo@DMN patch (10 × 10 array) was capable of withstanding a compression force of over 40 N, which is sufficient for penetration of human skin (Fig. 2G) [39–41]. Finally, Cy3@DMN inserted into an agarose gel released more than 90 % of the loaded Cy3 within 15 min, indicating its potential for rapid therapeutic delivery in cutaneous tissue.

2.4. Dual-responsive antimicrobial activity of Cu-Azo @DMN

The antimicrobial effect of the Cu-Azo@DMN was assessed against the planktonic and biofilm of Methicillin-resistant *Staphylococcus aureus* (MRSA) through the colony-forming unit assay. Without light stimulation, the Cu-Azo@DMN reduced the log-CFU by two-fold; however, with light stimulation, it led to a remarkable 4- log-CFU reduction (Fig. 3A–C). In contrast, the pure DMN didn't exhibit any notable antibacterial effect. Further, to elucidate the antimicrobial mechanism of Cu-Azo@DMN, its ROS generation ability was investigated using 3,3,5,5-tetramethylbenzidine (TMB) for detecting hydroxyl radicals (·OH) [42]. The fluorescence intensity at 652 nm, corresponding to TMB, was notably reduced after Cu-Azo@DMN treatment, and this reduction was more pronounced upon light irradiation. Next, 2, 2′-Bis-(anthracene-9,10-diylbis(methylene))-dimalonic acid (ABDA) probe was used to detect $^1O_2$, and the absorbance change at 380 nm was monitored continuously for 30 min [42]. The results showed that all groups with Cu-Azo@DMN produced $^1O_2$, with the highest production rate observed in the group with acidic pH and light stimulation (Fig. S10A and B). Therefore, our observations indicate that the burst release of Cu^{2+} triggered by acidic microenvironment and external light stimulation enhances the generation of various reactive oxygen species (ROS), such as singlet oxygen ($^1O_2$) and hydroxyl radicals (•OH), contributing to a potent broad-spectrum antimicrobial effect.

Subsequently, the destruction of the MRSA cell membrane by the light-triggered Cu-Azo@DMN was observed by SEM, whereas the cell membrane in the control group remained intact (Fig. 3D). Bicinchoninic acid (BCA) assay confirmed the cytosolic protein leakage from MRSA by Cu-Azo@DMN treatment (Fig. 3E) [42]. Additionally, we tested the antibacterial potency of Cu-azo degraded byproducts and found it effective against MRSA at pH 5.5 (Fig. S11A and B). Biphenyl derivatives also exhibited antibacterial properties by altering the hydrophobicity and net charge of the bacterial cell walls [43,44]. Nevertheless, using 2′, 7′-dichloro-dihydrofluorescein diacetate, we found that light-activated Cu-Azo@DMN significantly enhanced ROS production in MRSA, compared to the situation without light (Fig. 3F–S10C, D) [42,45].

We also investigated the impact of Cu-Azo@DMN on resilient fungal biofilms, which are generally more challenging to eradicate due to their thick cell membranes, rapid yeast-to-hyphae transformation, and effective quorum sensing [46,47]. Consequently, the efficacy of Cu-Azo@DMN against preformed biofilm of MRSA and *C. albicans* biofilms, which elicit acidic pH of 5.34 and 6.02, respectively (Fig. S11C). Light-activated Cu-Azo@DMN significantly reduced the CFU by 3-log, while Cu-Azo@DMN without light stimulation resulted in 1-1.5-log CFU reduction (Fig. 3G–I). Furthermore, XTT assay and CV-staining showed that light-activated Cu-Azo@DMN efficiently decreased the percentage of viable cells (<10 %) and significantly reduced total biofilm biomass compared to the control (Fig. 3J and K). Live/dead assay of MRSA biofilm also confirmed the excellent antibiofilm efficacy of the light-activated Cu-Azo@DMN (Fig. 3L). Next, we evaluated Cu-Azo@DMN efficacy on CA fungal biofilms, which are more challenging due to thick cell membranes and rapid yeast-to-hyphae transformation (Fig. S12A–D). Collectively, our data demonstrated the potent efficacy of light-activated Cu-Azo@DMN against bacterial and fungal biofilms.

2.5. Antimicrobial activity of Cu-Azo@DMN against cross-kingdom polymicrobial biofilm

The presence of polymicrobial cross-kingdom biofilm inhibits the effect of traditional antimicrobial agents [48,49]. Despite being one of the most common types of infection, the treatment strategies for the polymicrobial infection are very poorly understood to date due to the lack of proper in vitro and in vivo models [2,50]. Therefore, we examined the antimicrobial potency of Cu-Azo@DMN against the cross-kingdom polymicrobial biofilm formed by *S. aureus* (SA) and CA (Fig. 4A) [7]. CFU assay revealed that light-triggered Cu-Azo@DMN reduced log-CFU by more than 3-fold, while Cu-Azo@DMN alone exhibited limited antimicrobial activity (Fig. 4B and C). We also determined the cell viability of C. albicans and SA within biofilm after different treatments using an XTT assay. Compared with Cu-Azo@DMN without light stimulation, Cu-Azo@DMN stimulated with light contributed to a significantly greater decrease in cell viability (Fig. 4D). To investigate the effect of Cu-Azo@DMN on the biomass of biofilm, we studied the biofilm using CV staining. While Cu-Azo@DMN alone was able to reduce the biofilm biomass by ~50 %, light-stimulated Cu-Azo@DMN resulted in an even more outstanding reduction (>95 %) in biofilm biomass (Fig. 4E and F). Following SEM observation revealed that the cell walls of both the spherical-shaped SA and elongated hyphal CA were disrupted upon the light-stimulated Cu-Azo@DMN treatment (Fig. 4G).

Consequently, developing polymicrobial infection, including bacteria and fungi in vivo, is quite challenging [2,47]. Therefore, the antimicrobial performance of the Cu-Azo@DMN patch was tested in a clinically relevant ex vivo experiment comprised of dual-species microorganisms. In the current cross-kingdom dual-species ex vivo model, we have tested the pH and light-stimulated antimicrobial performance of the Cu-Azo@DMN in two different settings. In the one setup, we have used a 2-day-old dual-species suspension, which is acidic (pH~5.5) and in another, we have used a freshly inoculated microbial suspension, which has pH~7.4 (Fig. 4H). The ex vivo findings demonstrated that Cu-Azo@DMN combined with light exposure reduced microbial viability by 70 % in the 2-day-old biofilm at pH 5.5. In contrast, in the freshly prepared microbial suspension at near-neutral pH (7.4), the same treatment achieved 43.56 % eradication of both species (Fig. 4I–K).

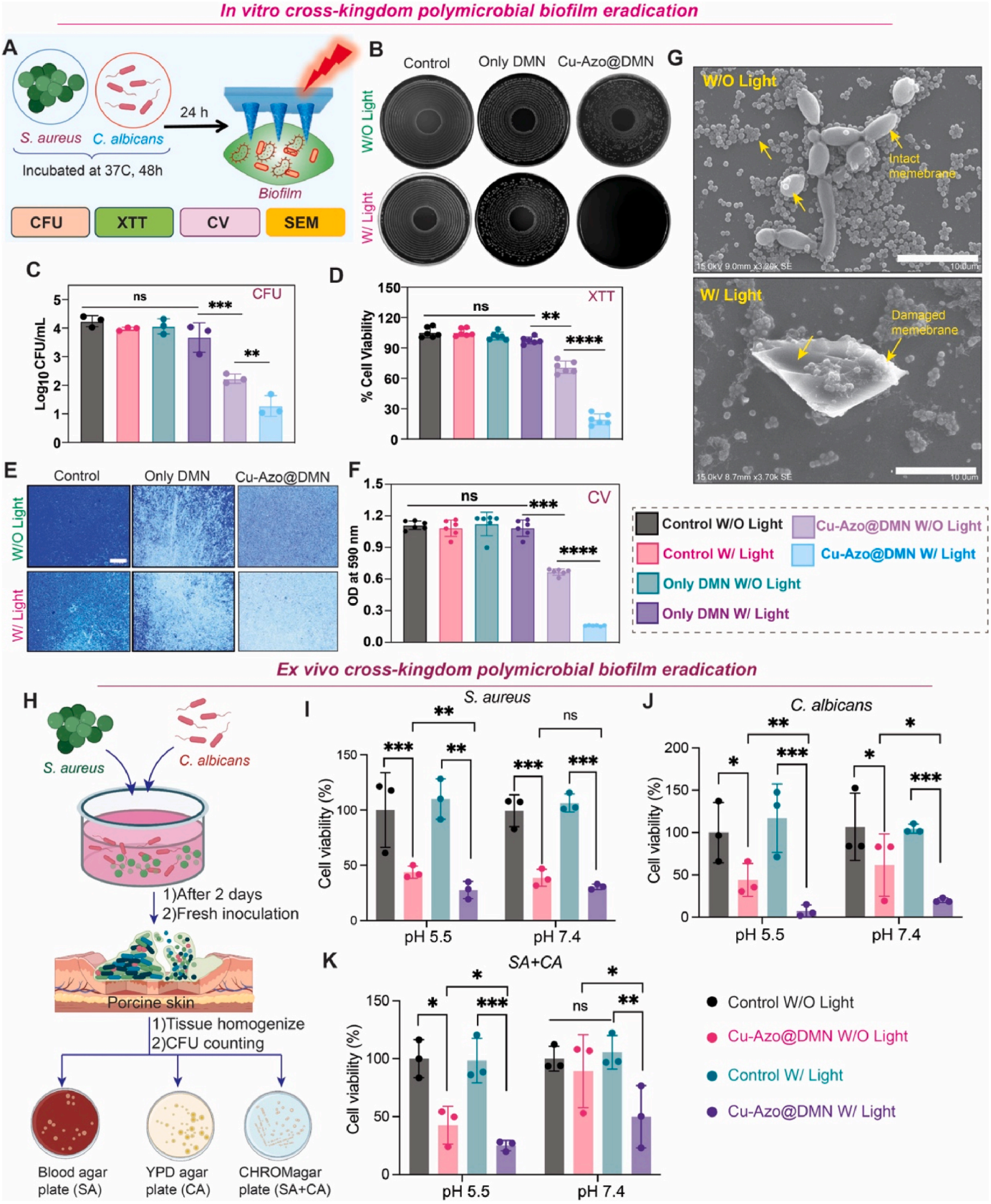

(caption on next page)

Fig. 4. Antimicrobial activity of Cu-Azo@DMN against cross-kingdom polymicrobial biofilm. (**A**) Schematic illustration of cross-kingdom dual-species polymicrobial biofilm, composed of *S. aureus* and *C. albicans,* development and treatment using Cu-Azo@DMN. Representative optical images (**B**) and corresponding statistical comparison (**C**) of CFU for cross-kingdom dual species biofilms of *C. albicans* and SA after different treatments (n = 3). (**D**) Quantifications of XTT assay for cell viability of *C. albicans* and SA within biofilm after different treatments. (**E**) Representative microscopic images, scale bar = 500 μm, and (**F**) corresponding quantification of CV staining for biofilms of *C. albicans* and SA (n = 6). (**G**) Representative SEM images of cross-kingdom biofilm after the treatment of Cu-Azo@DMN, scale bar = 10 μm. Cu-Azo@DMN promotes fibroblast recruitment and modulates macrophage polarization. (**H**) Schematic illustration of the development of ex vivo model for studying cross-kingdom infection using porcine skin. Microbial cell viability of (I) SA alone, (J) C. albicans alone, and (K) the C. albicans + SA dual-species biofilm after Cu-Azo@DMN treatment over the ex vivo dual-species biofilm, obtained from specific cultured plates, namely blood agar, YPD, and CHROMagar plates, respectively. (n = 3). Data were presented as mean ± SD. $*p < 0.05$, $**p < 0.01$, $***p < 0.001$.

These findings corroborated the superior antimicrobial performance of acidic pH-driven Cu-Azo@DMN against cross-kingdom polymicrobial infection under external light stimulation. However, the anti-microbial effects against other clinically relevant pathogens, such as isolates from infected human patients, would need to be tested to fully comprehend the therapeutic efficacy of Cu-Azo@DMN. Additionally, the use of UV light in this study might be an issue for a longer period; therefore, responsiveness to other wavelengths would be more beneficial.

2.6. Pro-regenerative properties of Cu-Azo@DMN

Following the eradication of microbial infection, cutaneous wound healing starts with the migration and proliferation of fibroblasts [1,9]. We first evaluated the biocompatibility of the Cu-Azo complex using human dermal fibroblasts (HDF). The cytotoxicity of the Cu-Azo complex demonstrated the biocompatible nature (>90 % viable) of the Cu-Azo complex in the 10–125 μg/mL concentration, regardless of light stimulation (Fig. S13A). Based on this result, 100 μg/mL of Cu-Azo complex was used for the Cu-Azo@DMN fabrication. CCK-8 assay showed that Cu-Azo@DMN contributed significantly higher cell viability than the control till 3 days (Fig. 5A). Scratch assay revealed that the Cu-Azo@DMN, regardless of light stimulation, accelerates HDF migration (Fig. 5B and C). Additionally, live/dead cell staining confirmed that Cu-Azo@DMN didn't affect HDF viability, even with light exposure (Fig. 5D–S13B). HDF cells treated with Cu-Azo@DMN extract medium showed increased F-actin and stretched stress fiber formation compared to the control and only DMN groups (Fig. 5E). These results consistently highlighted the excellent biocompatibility of Cu-Azo@DMN and its potential effects on accelerating migration and proliferation of dermal fibroblasts, independent of the light stimulation.

In the infectious wound environment, persistent oxidative stress, hypoxia, and the accumulation of immune cells such as macrophages, monocytes and neutrophils can lead to prolonged inflammation that impairs healing [1]. Considering the concentration-dependent effects of Cu^{2+} on immune responses, we anticipated that dual-responsive Cu-Azo@DMN could be utilised to regulate immunomodulatory functions [51,52]. Therefore, THP1 monocyte-derived macrophages were treated with Cu-Azo@DMN in acidic or neutral conditions, and the marker gene expressions were measured by RT-qPCR (Fig. 5F). At pH 5.5, genes encoding pro-inflammatory cytokines, such as interleukin-1β (*IL-1β*), tumour necrosis factor-α (*TNF-α*), prostaglandin E synthase (*PTGES*), and interleukin-8 (*IL-8*), were significantly upregulated (>3-fold) by the Cu-Azo@DMN (Fig. 5G). Light stimulation further upregulated these pro-inflammatory cytokines, resulting in pathogen clearance, immune cell recruitment and early differentiation of cells participating in wound healing processes [1,53]. However, at pH 7.4, Cu-Azo@DMN barely enhanced the expression of *IL-1β* and *TNF-α* unless triggered by light. Cu-Azo@DMN also led to the upregulation of *PTGES* and *IL-8* irrespective of light stimulation, which indicated the tissue regeneration effects of Cu-Azo@DMN by promoting innervation and vascularization of the cutaneous wound [54–56].

Additionally, Cu-Azo@DMN exhibited an anti-inflammatory response at pH 7.4 without light stimulation by significantly upregulating the expression of *CD206* and *IL-10* (Fig. 5G). Collectively, Cu-Azo@DMN effectively shifted its biological functions from pro-inflammation to anti-inflammation following the pH change in the wound microenvironment. Light stimulation is only necessary at the early infection stage, as it enhances the antimicrobial performance of Cu-Azo@DMN by amplifying the inflammatory responses in the acidic niche. These distinctive immunomodulatory effects of Cu-Azo@DMN arise from controlled Cu^{2+} release that modulates macrophage polarization in a concentration-dependent manner. During the initial infection phase with an acidic environment, light stimulation triggers a relatively higher concentration of Cu^{2+} from Cu-Azo@DMN (~33.4 μM after 4 h and 48.3 μM after 24 h), which lies within the therapeutic window for anti-infection (20 μM < X < 50 μM) [57]. At these levels, Cu^{2+} also promotes pro-inflammatory polarization of macrophages for infection eradication. Conversely, in the later healing phase, when the wound environment becomes neutral in pH, Cu^{2+} release from Cu-Azo@DMN reduces to a lower level (5.53 μM after 24 h and 9.22 μM after 72 h), which is optimal for anti-inflammatory modulation and pro-healing effects (<10 μM) [57].

Next, we examined the pro-regenerative angiogenic potential of the immune microenvironment by Cu-Azo@DMN [53,58]. Previous studies showed that pro-healing M2 macrophages can induce the angiogenesis process at the wound site [53]. Simultaneously, the migration of endothelial cells also indicated a positive hallmark for accelerated wound healing [1,2]. Cu-Azo@DMN significantly upregulated (>3 and 4-fold, respectively) the transforming growth factor (*TGF*) and vascular endothelial growth factor (*VEGF*) expression under both acidic and neutral conditions (Fig. 5G). TGF-β is well-known to facilitate fibroblasts-to-myofibroblasts differentiation by promoting F-actin stress fibers, α-smooth muscle actin, and large focal adhesions [59,60]. We further conducted a migration assay using Transwell to quantitatively assess the chemotactic response of human umbilical vein endothelial cells (HUVECs) to paracrine factors secreted by THP-1-derived macrophages. HUVECs were seeded in the upper insets and incubated in the conditioned medium from THP1-derived macrophages treated with and without Cu-Azo@DMN. Compared to the control group, the number of migrated HUVECs doubled when cultured in the conditioned medium from Cu-Azo@DMN treated macrophages, irrespective of light stimulation (Fig. 5H and I). Subsequently, the tube formation assay also demonstrated that the Cu-Azo@DMN induced angiogenesis, through a significantly increasing number of junctions, tubules, and length of tubules (Fig. 5J–M). Thus, upon infection eradication, Cu-Azo@DMN resolved inflammation through macrophage polarization and promoted the recruitment and differentiation of fibroblasts and endothelial cells to accelerate infected tissue regeneration. Moreover, our data consistently validated that during the early stages of wound infection, when a higher concentration of Cu^{2+} is beneficial, light can be exposed to accelerate ion release if needed. Conversely, in the later wound healing stages, when the pH is higher and Cu^{2+} release is naturally reduced, potentially limiting angiogenesis, irradiation can be used to enhance Cu^{2+} ion release and support the healing process.

3. Conclusion

Herein, we developed a dual-responsive copper complex for combating polymicrobial wound infection. The pH-responsive Schiff base linkages and light-sensitive azo moieties within the ligand framework enable precise control of Cu^{2+} according to the distinct needs at

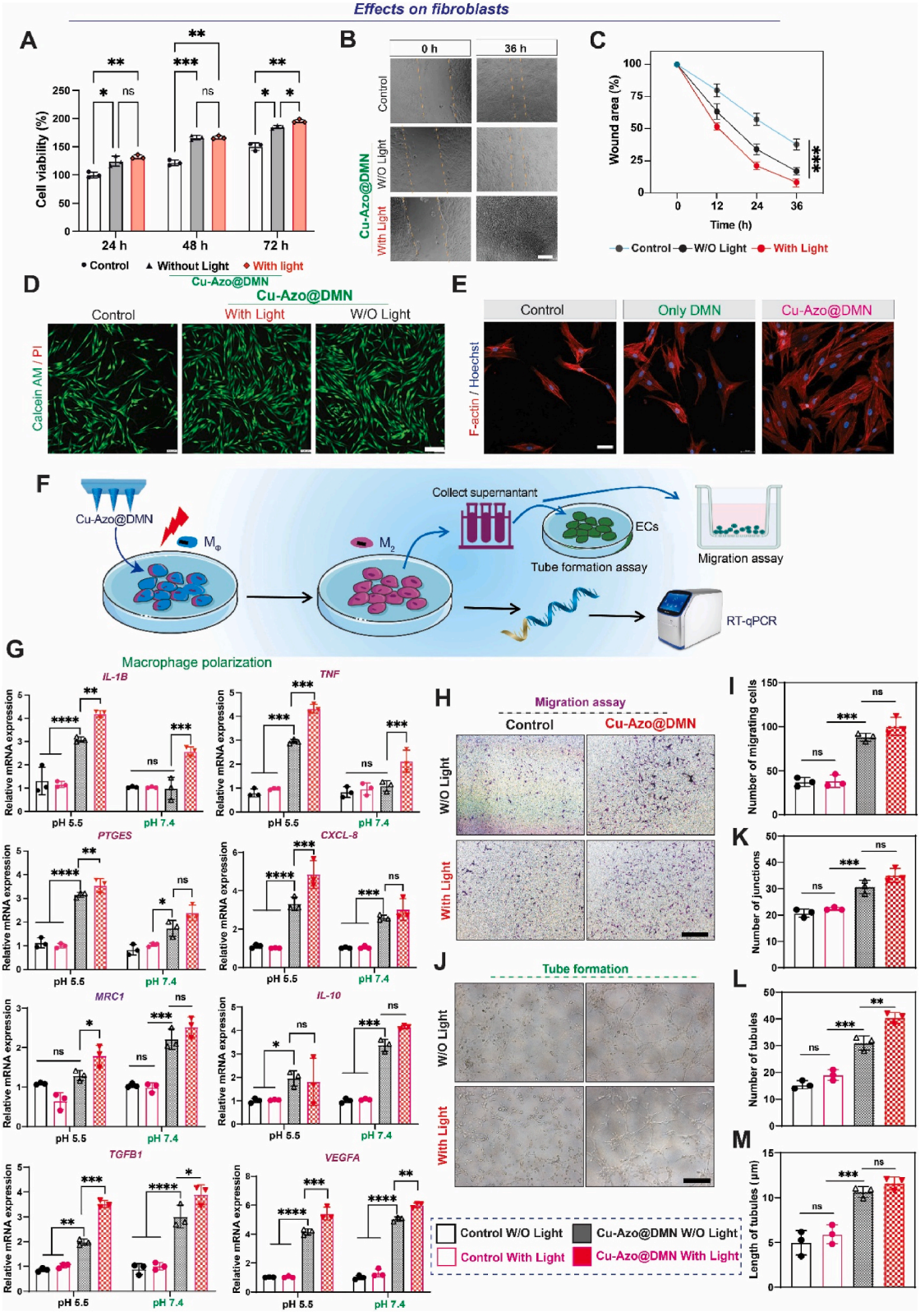

Fig. 5. Cu-Azo@DMN contributes to a pro-regenerative immune microenvironment. (A) Effect of Cu-Azo@DMN on HDF viability at days 1, 2, and 3 after coculture with Cu-Azo@DMN (with and without light stimulation). Representative optical images of the (**B**) scratch assay (scale bar = 100 μm) and (**C**) corresponding quantification for wound closure rate of HDFs. (**D**) Representative fluorescence images of live/dead assay of HDF at days 1, 2, and 3 after coculture (n = 3, scale bar = 200 μm). (**E**) Representative confocal microscopic images of HDFs with F-actin stained by Rhodamine-Phalloidin and nuclei stained by Hoechst with different treatments, scale bar = 50 μm. (**F**) Illustration of study design. (**G**) Relative expression levels of marker genes for polarization of THP1-derived macrophages after coculture. Representative optical microscopy images of (**H**) Transwell migration assay and (**I**) the number of migrated cells, (**J**) tube formation assay of HUVEC cells (scale bar = 250 μm). Corresponding quantification of (**K**) the number of junctions, (**L**) the number of tubules, and (**M**) the length of tubules of the HUVEC cells treated with conditioned medium. Data were presented as mean ± SD. $^{*}p < 0.05$, $^{**}p < 0.01$, $^{***}p < 0.001$.

different stages of infectious wound healing. Additionally, this design also allows tailored Cu^{2+} release in patients with diverse conditions for personalized medicine. Moreover, the Cu-Azo complex was incorporated into a dissolvable microneedle system for pain-free transdermal delivery. Cu-Azo@DMN exhibited excellent antimicrobial potency against cross-kingdom polymicrobial biofilms, with enhanced efficacy under external light stimulation. Following the infection eradication, reduced Cu^{2+} release from Cu-Azo@DMN shifted its immunomodulatory effect from pro-inflammatory to pro-regenerative, promoting fibroblast recruitment and angiogenesis. Conclusively, our study demonstrated dual-responsive Cu-Azo@DMN as a promising multifunctional therapeutic platform for the treatment of infectious wounds with improved therapeutic efficacy.

4. Experimental section

4.1. Materials

Gelatin from porcine skin (300 g bloom) and sodium alginate were purchased from Macklin Biochemical Technology (Shanghai, China). 2,2′-Bis-(anthracene-9,10-diylbis(methylene))-dimalonic acid (ABDA) and 3,3,5,5′-tetramethylbenzidine (TMB) were obtained from Aladdin Biochemical Technology (Shanghai, China). Bicinchoninic acid (BCA) kit and 2′,7′-dichloro-dihydrofluorescein diacetate (DCFH-DA) were obtained from Beyotime Biotechnology Co., Ltd. (Shanghai, China). Dulbecco's modified Eagle medium (DMEM), Roswell Park Memorial Institute Medium (RPMI-1640), Endothelial Cell Growth Medium, 10 % Fetal Bovine Serum (FBS), 0.25 % trypsin−ethylenediaminetetraacetic acid (EDTA), and penicillin−streptomycin (PS) were obtained from Gibco, Thermofisher Scientific, USA. All chemicals were used as received.

4.2. Fabrication of Cu-Azo@DMN patch

The Cu-Azo@DMN was fabricated using a two-step micromolding process, as previously described [39]. Firstly, a PDMS mold was created using a pyramidal stainless-steel master mold containing 100 needles arranged in a 10 × 10 array (Micropoint Technologies Pvt. Ltd., Singapore). Each needle had a height of 700 μm, a tip radius of 5 μm, and a base width of 300 μm. The PDMS mold was prepared by pouring a 10:1 ratio of PDMS prepolymer solution over the steel master mold, followed by degassing in a vacuum chamber to remove air bubbles. The PDMS was then cured by heating at 70 °C for 2 h, after which the negative mold was carefully peeled off from the master mold.

For the fabrication of dissolvable microneedles (DMNs), a base polymer system composed of gelatin and sodium alginate (SA) was utilised. Briefly, 750 mg of gelatin and 250 mg of SA were thoroughly mixed with 1 mL of PBS to form a homogeneous polymer suspension. Subsequently, 400 μL of the polymer solution was poured into the PDMS mold and centrifuged at 3000 rpm for 5 min to ensure complete filling of the microneedle cavities and to eliminate trapped air. A second layer of the polymer solution was then added to form the backing layer of the patch. The DMNs were air-dried for 3 days at room temperature and gently peeled off from the PDMS mold.

Similarly, Cu-Azo@DMN and Cy-3@DMN were also fabricated using the same procedure, followed by the addition of 100 μg/mL of the Cu-Azo complex or 0.5 μg/mL of Cy-3 dye to the polymer suspension before molding.

4.3. Characterizations of Cu-Azo@DMN

The surface morphology of the prepared Cu-Azo@DMN was examined using Scanning electron microscopy (SEM, Hitachi Co. Ltd., Japan) and the successful entrapment of the Cu-Azo complex inside the DMN was examined through the elemental analysis by using EDX analysis.

4.4. Mechanical testing of Cu-Azo@DMN

The mechanical strength of the Cu-Azo@DMN was determined through a compression test using an Instron 5543 Tensile meter. The MN patches were positioned with their tips facing upward on a flat stainless-steel platform. A compressive force was applied perpendicularly to the patches at a constant rate of 0.5 mm/min. The displacement of the needles was measured under a preset maximum force limit of 50 N per patch.

4.5. Ex vivo skin penetration test

A fresh porcine ear model was utilised to evaluate the skin puncture ability of the fabricated microneedles [39]. Briefly, a fresh porcine ear was obtained from a local slaughterhouse and thoroughly washed with PBS to remove hair and surface debris. Subsequently, a Cy-3@ DMN patch was applied to the ear skin using a force of 1.5 N for 1 min to ensure proper insertion. Following application, the tissue specimens with inserted microneedles were immediately frozen using optimal cutting temperature (OCT) compound. Cross-sectional slices of 5 μm thickness were prepared using a microtome. Finally, the skin specimens were visualized under a fluorescence microscope (Zeiss Axio Observer Z1, Carl Zeiss, Germany) to assess the distribution and penetration of the Cy-3@DMNs within the tissue.

4.6. In vitro antimicrobial activity test

The antimicrobial of Cu-Azo@DMN was evaluated against both planktonic cultures and biofilms using three model organisms: *Staphylococcus aureus* (ATCC 25923), Methicillin-resistant *Staphylococcus aureus* (MRSA, ATCC 700698), and *Candida albicans* (ATCC SC5314). Briefly, *S. aureus* and MRSA were cultured overnight in Tryptic-Soy Broth (TSB) medium, while *C. albicans* was cultured in Yeast Peptone Dextrose (YPD) medium, under shaking conditions at 37 °C (5 % CO_2, 45 % humidity). The cultures were then centrifuged at 6000 rpm for 10 min, and the resulting pellets were resuspended in PBS to achieve a uniform microbial concentration of approximately 1×10^6 colony-forming units per millilitre (CFU/mL).

For the antimicrobial activity assays, soaked solutions of Cu-Azo@DMN were prepared by incubating the microneedles in 1 mL of PBS for 24 h, with and without light exposure. Concurrently, microbial cultures were prepared in their respective media. The soaked solutions of the Cu-Azo@DMN was prepared by immersing it in PBS with (365 nm, 5 min, 5 mW/cm^2) and without light stimulation. Subsequently, 100 μL of the soaked Cu-Azo@DMN solutions were co-cultured with 1×10^6 CFU/mL of each microorganism and incubated for 24 h at 37 °C (5 % CO_2, 45 % humidity). After incubation, the optical density (OD) of the cultures was measured using a UV–visible spectrophotometer at 660 nm for *S. aureus* and MRSA, and at 520 nm for *C. albicans*, to assess microbial growth inhibition.

For CFU assessment, 10 μL of the treated microbial suspensions were serially diluted 10^3-fold in PBS. Then, 50 μL of the diluted suspensions were spread onto blood agar plates (for *S. aureus* and MRSA or YPD agar plates (for *C. albicans*) using a spiral plater (Bioscience, USA). The plates were incubated at 37 °C for 24 h, after which the number of colonies was counted to quantify viable cells.

Additionally, to evaluate the anti-biofilm activity, biofilms of MRSA and *C. albicans* were established by inoculating 5×10^6 cells/mL in 24-well plates and incubating for 48 h. The anti-biofilm experiments were conducted following the same protocol as described for the planktonic cultures.

4.7. Crystal violet (CV) staining

The biofilm biomass of the different biofilms after Cu-Azo@DMN treatments was quantified using the Crystal violet assay. Briefly, pre-

formed biofilms of MRSA and Candida albicans were established over three days by inoculating 1 × 10^6 cells/mL in TSB and YPD medium, respectively, in 24-well plates [42]. After biofilm formation, the wells were gently washed with PBS to remove unattached cells, followed by the application of the respective treatments. The treated biofilms were then incubated at 37 °C for 24 h. Following incubation, the supernatant was carefully removed, and the biofilms were washed three times with PBS to eliminate residual media and non-adherent cells. The wells were air-dried completely for 20–30 min, after which 1 % CV solution was added to each well and allowed to stain the biofilms for 20 min. The CV solution was then aspirated, and the wells were rinsed twice with PBS to remove excess stain. The plates were air-dried once again, and the stained biofilms were solubilized using 33 % acetic acid. Finally, the absorbance of the dissolved crystal violet was measured at 595 nm using a multi-plate reader to quantify the biofilm biomass.

4.8. XTT assay

To quantify the viable cells inside the biofilm matrix, an XTT reduction assay was performed. In brief, after the antibiofilm experiment steps, 100 μL of treated microbial biofilm suspensions were mixed with 10 μL of XTT solution, and the plate was incubated at 37 °C for 3 h in the dark. Following incubation, 100 μL of the suspension was transferred into a new sterile 96-well plate, and the absorbance at 450 nm wavelength was measured using a microtiter plate reader.

4.9. Protein leakage assay

After different Cu-Azo@DMN treatments, the MRSA cell suspension was centrifuged to obtain the supernatant, then 15 μL of the supernatant was mixed with 200 μL of enhanced BCA assay kit (Beyotime, China) and the mixture was incubated in a shaker at 37 °C for 30 min. OD value was observed at an emission wavelength of 562 nm.

4.10. SEM analysis of bacterial membrane

Furthermore, to verify the deformed cell membrane by SEM, after the different treatments for 24 h, 10 μL of bacterial cell suspensions were taken on a glass slide, fixed with ice-cold 2.5 % glutaraldehyde, followed by dehydration with ethanol gradient and observed under SEM (Shimadzu, Japan) [42,61].

4.11. In vitro ROS detection

To validate the ROS production with the application of Cu-Azo@DMN under light exposure, we have done a DCFH-DA-based fluorometric assay [42]. In brief, MRSA cells (1 × 10^6 cells/mL) were cultured in 10 mm confocal Petri dishes for 12 h at 37 °C. Then, the 200 μL soaked solutions of Cu-Azo@DMN with and without light exposure were added to each well for another 12 h. After being gently washed with PBS (pH 7.4) in triplicate, 10 μM DCFH-DA was added to each well, followed by 30 min incubation in the dark. After 30 min, cells were gently washed with fresh medium and observed under the fluorescence microscope at a 488 nm laser. The fluorescence intensity of ROS was measured by using ImageJ software.

4.12. Antimicrobial activity test against cross-kingdom polymicrobial biofilm in vitro

A bacteria-fungi dual-species biofilm was prepared to evaluate the antimicrobial activity of Cu-Azo@DMN against cross-kingdom polymicrobial biofilm [7,62,63]. Briefly, *C. albicans* and *S. aureus* cell suspensions were adjusted to 1 × 10^6 cells/mL in RPMI 1640 medium, and 100 μl of the cell suspensions were added to 24-well polystyrene flat-bottom plates. Plates were incubated for 12 h at 37 °C, and then wells were washed twice with PBS to remove nonadherent cells. Fresh medium (200 μL) was added to each well, and biofilms were allowed to form for 48 h at 37 °C. Following incubation, wells were washed with PBS. After that, different soaked solutions of Cu-Azo@DMN with and without light exposure were treated on the mixed-species biofilm and incubated for 24 h. After that, CFU counting, CV staining and XTT assay were performed following the above procedures. For CFU counting, CHROMagar plates were used to grow the dual species.

4.13. Ex vivo antimicrobial activity test

The ex vivo cross-kingdom dual-species model was developed to test the pH and light-stimulated antimicrobial performance of the Cu-Azo@DMN in two different settings. In the one chamber slide, we have grown a 2-day-old dual-species culture comprised of *C. albicans* and *S. aureus* cell suspensions (1 × 10^6 cells/mL) in RPMI-1640 medium, which is acidic (pH~5.5). Meanwhile, we also used a freshly inoculated dual-species suspension, which has pH~7.4. After that, the freshly collected porcine skins were prepared by repetitive washing with PBS, and then a hole was created using an 8 mm biopsy punch; after that the 200 μL of microbial suspension was inoculated. After applying the respective treatments, the skin tissues were homogenized and diluted with PBS. For the CFU counting, 3 different kinds of CFU plates were used, namely blood agar plates specific to *S. aureus*, YPD plates for only *C. albicans* and a specialised chromogenic plate (CHROMagar; DRG International, USA) for specific detection of both microorganisms.

4.14. Cell culture

Human dermal fibroblasts, THP-1 and human umbilical vein endothelial cells (HUVECs) cell lines were obtained from the American Type Culture Collection (ATCC). HDF was cultured in DMEM supplemented with 10 % FBS and 1 % Penicillin-Streptomycin solution at 37 °C (95 % humidity, 5 % CO_2), whereas THP-1 cells were cultured in RPMI 1640 medium supplemented with 10 % FBS. HUVECs were cultured in Endothelial Cell Growth Medium with 10 % FBS at 37 °C (95 % humidity, 5 % CO_2).

4.15. Biocompatibility and live/dead assay

The cytocompatibility of Cu-Azo@DMN was evaluated with human dermal fibroblast (HDF) cells using the Cell Counting Kit-8 (CCK-8) assay. To prepare the treatment solutions, Cu-Azo@DMN patches were soaked in serum-free Dulbecco's Modified Eagle Medium (DMEM) for 24 h, both with and without light irradiation (365 nm, 5 mW/cm^2, 5 min). The resulting soaked solutions were collected and used for subsequent cell-based assays.

For the cell viability assay, HDF cells were seeded at a density of 1 × 10^5 cells per well in a 24-well plate and incubated for 24 h to allow monolayer formation. Concurrently, soaked solutions of the Cu-Azo@DMN patches were prepared by submerging the patches in serum-free DMEM for 24 h. After monolayer formation, 500 μL of the medium containing the soaked solutions was added to each well, and the cells were incubated for an additional 24 h at 37 °C. Following incubation, the medium was removed, and 300 μL of CCK-8 solution (Life Technologies, Singapore) was added to each well. The plates were then incubated in the dark for 1 h. Cell viability and proliferation were assessed by measuring the optical absorbance of each well at 24, 48, and 72 h using the CCK-8 kit (Beyotime, China). Furthermore, Calcein AM/PI-staining method was used to observe the live cells [64]. Briefly, 10 μL of the staining solution was added directly to the wells containing treated cells, followed by incubation at 37 °C for 30 min. The stained cells were then observed under a confocal microscope to distinguish live (Calcein AM-positive) and dead (PI-positive) cells.

4.16. Scratch assay

HDF cells (1×10^5 cells/well) were seeded into 6-well plates for 24 h under a 5 % CO_2 atmosphere. After cells reached 80 % confluency, a vertical scratch was made in each well using the tip of a 200 μL pipette tips, and then the soaked solutions of Cu-Azo@DMN with and without light exposure were added and incubated for 24 h. At the predetermined time points, optical images of the well were taken and quantified using the ImageJ software.

4.17. Cytoskeleton staining

To observe the cytoskeleton remodelling, HDF cells (1×10^4 cells/well) were seeded into 24-well plates for 24 h under a 5 % CO_2 atmosphere. After the adhesion, the complete medium was exchanged with the soaked solution of Cu-Azo@DMN for another 24 h. Then, the fibroblasts in each group were fixed with 4 % PFA for 15 min and stained with rhodamine-phalloidin for 30 min, followed by 10 min of Hoechst staining [65]. The cell morphology and lamellipodia were observed using the confocal microscope.

4.18. Real-time quantitative polymerase chain reaction (RT-qPCR)

To examine the immunoregulatory effects of Cu-Azo@DMN, we performed RT-qPCR. HP-1 cells were differentiated into macrophages by culturing them in serum-free RPMI 1640 medium supplemented with 10 ng/mL phorbol-12-myristate-13-acetate (PMA, Sigma-Aldrich) for 48 h [66]. Following differentiation, the THP-1-derived macrophages were co-cultured with Cu-Azo@DMN patches, both with and without light irradiation (365 nm, 5 mW/cm^2, 5 min), and incubated for an additional 48 h [53]. After incubation, total RNA was extracted from the treated cells using the RNeasy Mini Kit (Qiagen, Hilden, Germany), and RNA purity was assessed using a NanoDrop spectrophotometer (Thermo Fisher Scientific, USA). The extracted RNA was then reverse transcribed into complementary DNA (cDNA) using the First Strand cDNA Synthesis Kit (Takara, Dalian, China). Real-time quantitative PCR was performed using TB Green Premix (Takara, Japan) on a qPCR instrument. The mean cycle threshold (C_t) values of target genes were normalized to the housekeeping gene GAPDH to account for variations in RNA input and cDNA synthesis efficiency. The primer sequences for the target genes are provided in Table S2.

4.19. Cell migration assay

To investigate whether Cu-Azo contributes to skin healing through stimulating macrophage paracrine secretions, the conditioned medium from the culture medium of Cu-Azo@DMN-treated macrophages was prepared. Briefly, macrophages were differentiated from THP1 cells using serum-free RPMI 1640 supplemented with 10 ng/mL phorbol-12-myristate-13-acetate (PMA, Sigma-Aldrich). Following differentiation, the macrophages were treated with soaked solutions of Cu-Azo@DMN at pH 7.4 without any light stimulation, and culture supernatants were collected after 48 h. The collected medium was centrifuged at 12,000 rpm for 15 min to remove cell debris and particulate matter, sterilized using a 0.22 μm filter, and stored at −80 °C until further use.

The migratory capacity of human umbilical vein endothelial cells (HUVECs) was assessed using a Transwell migration assay [64]. In brief, HUVECs (5×10^4 cells/well) were cultured in the upper chamber of the Transwell inserts (Corning, USA), and a different conditioned medium was added in the lower chamber. After 12 h of incubation, the membranes containing migrated cells were carefully removed, fixed with 4 % paraformaldehyde, and stained with 0.1 % crystal violet. The stained cells were visualized under a microscope (Zeiss, Germany), and the number of migrated cells was quantified to evaluate the chemotactic effect of the conditioned media.

For the tube formation test, the 24-well plates were first coated with 200 μL of Matrigel and incubated for 30 min in a 37 °C incubator. After that, the HUVECs treated with Cu-Azo@DMN were seeded on top of the Matrigel coating. The formation of tubules was observed after 4 h by an optical microscope, and the number, lengths and junctions of tubules were quantified by Image Pro Plus software [64].

4.20. Statistical analysis

All the above experiments were performed in triplicate manner under the same conditions independently. All experimental data are shown as the mean ± standard deviation. The statistical analysis of the data is carried out using GraphPad Prism 8.4.2 and Origin 2016 software. Ordinary one-way or two-way analysis of variance (ANOVA) was performed depending on the number of variables. They were followed by Šídák's or Tukey's test for multiple comparisons for two or more groups, respectively. In the two-way ANOVA, only simple effects within rows and columns are analyzed. The differences between the two groups were calculated through Student's T-test. Differences between different groups at mean ± SD. $*p < 0.05$, $**p < 0.01$, $***p < 0.001$ were considered statistically significant.

CRediT authorship contribution statement

Sumanta Ghosh: Writing – original draft, Visualization, Methodology, Investigation, Formal analysis, Data curation, Conceptualization. **Soumen Ghosh:** Writing – original draft, Methodology, Investigation, Formal analysis, Data curation. **Kelvin W.K. Yeung:** Methodology, Investigation. **Chenjie Xu:** Methodology, Investigation. **Jun Wu:** Methodology, Investigation. **Congyang Mao:** Methodology, Investigation. **Zemin Ling:** Methodology, Investigation. **Kou Okuro:** Supervision, Methodology. **Wei Qiao:** Writing – review & editing, Writing – original draft, Validation, Supervision, Resources, Project administration, Investigation, Funding acquisition, Conceptualization.

Funding sources

The work is supported by funding from the Research Grants Council, the Government of the Hong Kong SAR (Collaborative Research Fund No.C7003-22Y and General Research Fund No.17118425 to W.Q.), the Food and Health Bureau, the Government of the Hong Kong SAR (No.09201466 to W.Q.), National Natural Science Foundation of China (No.82201124 to W.Q.), National Natural Science Foundation of China/Research Grants Council Joint Research Scheme (N_HKU721/23 to W.Q.); Hong Kong Innovation Technology Fund (ITS/256/22 to W.Q.), Shenzhen Science and Technology Innovation Committee Projects (Nos. SGDX20220530111405038, W.Q.), Guangdong Basic and Applied Basic Research Foundation (2023A1515011963, W.Q.), National Natural Science Foundation of China (82102520 to Z.L.).

Declaration of competing interest

The authors declare that they have no known competing financial interests or personal relationships that could have appeared to influence the work reported in this paper.

Acknowledgement

The authors thank the Central Research Laboratory, the Faculty of Dentistry and the Department of Chemistry at the University of Hong Kong for their immense technical help with the experiments. We would also like to thank Ms. Shanthini Kalimuthu for her immense support throughout the work.

Supporting Information

Additional experimental details, including synthesis procedures, ion

release study, NMR, Mass, EDX analysis, PXRD, and XPS. Diffraction parameters and primer sequences for RT-qPCR study (PDF).

Appendix A. Supplementary data

Supplementary data to this article can be found online at https://doi.org/10.1016/j.mtbio.2025.102219.

Data availability

Data will be made available on request.

References

[1] O.A. Peña, P. Martin, Cellular and molecular mechanisms of skin wound healing, Nat. Rev. Mol. Cell Biol. (2024) 1–18.

[2] A. Uberoi, A. McCready-Vangi, E.A. Grice, The wound microbiota: microbial mechanisms of impaired wound healing and infection, Nat. Rev. Microbiol. (2024) 1–15.

[3] F. Mariani, E.M. Galvan, Staphylococcus aureus in polymicrobial skinand soft tissue infections: impact of inter-species interactionsin disease outcome, Antibiotics (Basel) 12 (7) (2023).

[4] A. Frei, A.D. Verderosa, A.G. Elliott, J. Zuegg, M.A. Blaskovich, Metals to combat antimicrobial resistance, Nat. Rev. Chem 7 (3) (2023) 202–224.

[5] C.S. Ho, C.T. Wong, T.T. Aung, R. Lakshminarayanan, J.S. Mehta, S. Rauz, A. McNally, B. Kintses, S.J. Peacock, C. de la Fuente-Nunez, Antimicrobial resistance: a concise update, Lancet Microbe 6 (1) (2024) 100947.

[6] D.L. Allison, H.M. Willems, J. Jayatilake, V.M. Bruno, B.M. Peters, M.E. Shirtliff, Candida–bacteria interactions: their impact on human disease, Virulence Mechanisms of Bacterial Pathogens (2016) 103–136.

[7] E.F. Kong, C. Tsui, S. Kucharíková, D. Andes, P. Van Dijck, M.A. Jabra-Rizk, Commensal protection of Staphylococcus aureus against antimicrobials by Candida albicans biofilm matrix, mBio 7 (5) (2016), https://doi.org/10.1128/mbio.01365-16.

[8] F.A. Olivier, V. Hilsenstein, H. Weerasinghe, A. Weir, S. Hughes, S. Crawford, J. E. Vince, M.J. Hickey, A. Traven, The escape of Candida albicans from macrophages is enabled by the fungal toxin candidalysin and two host cell death pathways, Cell Rep. 40 (12) (2022).

[9] W. Fu, S. Sun, Y. Cheng, J. Ma, Y. Hu, Z. Yang, H. Yao, Z. Zhang, Opportunities and challenges of nanomaterials in wound healing: advances, mechanisms, and perspectives, Chem. Eng. J. (2024) 153640.

[10] R. Jamaledin, C.K. Yiu, E.N. Zare, L.N. Niu, R. Vecchione, G. Chen, Z. Gu, F.R. Tay, P. Makvandi, Advances in antimicrobial microneedle patches for combating infections, Advanced materials 32 (33) (2020) 2002129.

[11] E.J. González López, Y.B. Palacios, S.R. Martinez, A.M. Durantini, E.N. Durantini, G.A. Abraham, S. Bongiovanni Abel, D.A. Heredia, Light-activated antibacterial ethylcellulose electrospun nanofibrous mats containing fluorinated Zn (II) porphyrin, ACS Appl. Polym. Mater. 6 (13) (2024) 7691–7704.

[12] G. Liu, R. Xia, M. Gui, L. Zhang, X. Zhou, J. Xue, Y. Cai, Y. Cao, Y. Xiao, Z. Chen, Turn hood into good: recycling silicon from mesoporous silica nanoparticles through magnesium modification to lower toxicity and promote tissue regeneration, ACS Nano 18 (47) (2024) 32932–32949.

[13] K. Cutting, R. White, M. Edmonds, The safety and efficacy of dressings with silver–addressing clinical concerns, Int. Wound J. 4 (2) (2007) 177–184.

[14] H. Ali, E. Khan, I. Ilahi, Environmental chemistry and ecotoxicology of hazardous heavy metals: environmental persistence, toxicity, and bioaccumulation, J. Chem. 2019 (1) (2019) 6730305.

[15] R.J. Turner, The good, the bad, and the ugly of metals as antimicrobials, Biometals 37 (3) (2024) 545–559.

[16] P. Wang, Y. Yuan, K. Xu, H. Zhong, Y. Yang, S. Jin, K. Yang, X. Qi, Biological applications of copper-containing materials, Bioact. Mater. 6 (4) (2021) 916–927.

[17] O. Gorel, M. Hamuda, I. Feldman, I. Kucyn-Gabovich, Enhanced healing of wounds that responded poorly to silver dressing by copper wound dressings: prospective single arm treatment study, Health Sci. Rep. 7 (1) (2024) e1816.

[18] A. Lončarević, Z. Malbaša, M. Kovačić, K. Ostojić, A. Angaïts, Ž. Skoko, J. Szpunar, I. Urlić, G.G. Ferrer, A. Rogina, Copper–Zinc/Chitosan complex hydrogels: rheological, degradation and biological properties, Int. J. Biol. Macromol. 251 (2023) 126373.

[19] S.M. Imani, L. Ladouceur, T. Marshall, R. Maclachlan, L. Soleymani, T.F. Didar, Antimicrobial nanomaterials and coatings: current mechanisms and future perspectives to control the spread of viruses including SARS-CoV-2, ACS Nano 14 (10) (2020) 12341–12369.

[20] L. Gao, A. Zhang, Copper-instigated modulatory cell mortality mechanisms and progress in oncological treatment investigations, Front. Immunol. 14 (2023) 1236063.

[21] K. Li, C. Xia, Y. Qiao, X. Liu, Dose-response relationships between copper and its biocompatibility/antibacterial activities, J. Trace Elem. Med. Biol. 55 (2019) 127–135.

[22] M. Vincent, R.E. Duval, P. Hartemann, M. Engels-Deutsch, Contact killing and antimicrobial properties of copper, J. Appl. Microbiol. 124 (5) (2018) 1032–1046.

[23] D. Mitra, E.-T. Kang, K.G. Neoh, Antimicrobial copper-based materials and coatings: potential multifaceted biomedical applications, ACS applied materials & interfaces 12 (19) (2019) 21159–21182.

[24] Y. Zu, Y. Wang, H. Yao, L. Yan, W. Yin, Z. Gu, A copper peroxide Fenton nanoagent-hydrogel as an in situ pH-responsive wound dressing for effectively trapping and eliminating bacteria, ACS Appl. Bio Mater. 5 (4) (2022) 1779–1793.

[25] P. Makvandi, U. Josic, M. Delfi, F. Pinelli, V. Jahed, E. Kaya, M. Ashrafizadeh, A. Zarepour, F. Rossi, A. Zarrabi, Drug delivery (nano) platforms for oral and dental applications: tissue regeneration, infection control, and cancer management, Adv. Sci. 8 (8) (2021) 2004014.

[26] S. Ono, R. Imai, Y. Ida, D. Shibata, T. Komiya, H. Matsumura, Increased wound pH as an indicator of local wound infection in second degree burns, Burns 41 (4) (2015) 820–824.

[27] R. Derwin, D. Patton, H. Strapp, Z. Moore, Wound pH and temperature as predictors of healing: an observational study, J. Wound Care 32 (5) (2023) 302–310.

[28] A.B.D. Nandiyanto, R. Ragadhita, M. Fiandini, Interpretation of fourier transform infrared spectra (FTIR): a practical approach in the polymer/plastic thermal decomposition, Indonesian Journal of Science and Technology 8 (1) (2023) 113–126.

[29] A. Baby, A.M. John, S.P. Balakrishnan, Photoresponsive carbon-azobenzene hybrids: a promising material for energy devices, ChemPhysChem 24 (6) (2023) e202200676.

[30] J. Konieczkowska, D. Neugebauer, A. Kozanecka-Szmigiel, A. Mazur, S. Kotowicz, E. Schab-Balcerzak, Photoresponse of new azo pyridine functionalized poly (2-hydroxyethyl methacrylate-co-methyl methacrylate), Sci. Rep. 14 (1) (2024) 9078.

[31] Y. Huang, L. Shen, D. Guo, W. Yasen, Y. Wu, Y. Su, D. Chen, F. Qiu, D. Yan, X. Zhu, A NIR-triggered gatekeeper of supramolecular conjugated unimicelles with two-photon absorption for controlled drug release, Chem. Commun. 55 (47) (2019) 6735–6738.

[32] X. Zhou, Y. Chi, J. Yang, P. Yin, Photoresponsive viscoelasticity of the granular materials of azobenzene-bearing molecular nanoparticles, ACS Appl. Mater. Interfaces 16 (15) (2024) 19563–19570.

[33] H.D. Bandara, S.C. Burdette, Photoisomerization in different classes of azobenzene, Chem. Soc. Rev. 41 (5) (2012) 1809–1825.

[34] K. Yabuuchi, T. Katsumata, T. Shimoboji, Y. Hashimoto, T. Kimura, K. Akiyoshi, A. Kishida, Variable swelling behavior of and drug encapsulation in a maleimide-modified hyaluronic acid nanogel-based hydrogel, Polym. J. 56 (5) (2024) 505–515.

[35] A. Johnson, F. Kong, S. Miao, H.-T.V. Lin, S. Thomas, Y.-C. Huang, Z.-L. Kong, Therapeutic effects of antibiotics loaded cellulose nanofiber and κ-carrageenan oligosaccharide composite hydrogels for periodontitis treatment, Sci. Rep. 10 (1) (2020) 18037.

[36] H. Li, L. Vora, Y. Li, A.K. Pandya, J. Wang, Y. Luo, A.M. Abraham, E.B. Guix, E. Riveira, M. Nevot, Transdermal delivery of enfuvirtide using dissolving microneedles integrated with novel insertion and removal indicator, J. Contr. Release (2025) 113954.

[37] N.N. Al-Rawi, M. Rawas-Qalaji, Dissolving microneedles with antibacterial functionalities: a systematic review of laboratory studies, Eur. J. Pharmaceut. Sci. 174 (2022) 106202.

[38] R. Xie, D. Fan, Y. Fang, T. Zhu, H. Li, Y. Yin, X. Liu, Y. Ma, F. Chen, W. Zeng, Dissolving microneedles embedded with photosensitizers for targeted eradication of gram-positive bacteria in multidrug-resistant biofilms in diabetic wound infections, Adv. Healthcare Mater. (2025) 2405190.

[39] R.Z. Seeni, M. Zheng, D.C.S. Lio, C. Wiraja, M.F.B. Mohd Yusoff, W.T.Y. Koh, Y. Liu, B.T. Goh, C. Xu, Targeted delivery of anesthetic agents to bone tissues using conductive microneedles enhanced iontophoresis for painless dental anesthesia, Adv. Funct. Mater. 31 (47) (2021) 2105686.

[40] S. Ghosh, M. Zheng, J. He, Y. Wu, Y. Zhang, W. Wang, J. Shen, K.W. Yeung, P. Neelakantan, C. Xu, Electrically-driven drug delivery into deep cutaneous tissue by conductive microneedles for fungal infection eradication and protective immunity, Biomaterials 314 (2025) 122908.

[41] S.P. Davis, B.J. Landis, Z.H. Adams, M.G. Allen, M.R. Prausnitz, Insertion of microneedles into skin: measurement and prediction of insertion force and needle fracture force, J. Biomech. 37 (8) (2004) 1155–1163.

[42] X. Zhao, L. Chang, Y. Hu, S. Xu, Z. Liang, X. Ren, X. Mei, Z. Chen, Preparation of photocatalytic and antibacterial MOF nanozyme used for infected diabetic wound healing, ACS Appl. Mater. Interfaces 14 (16) (2022) 18194–18208.

[43] H.A. Ali, M.A. Ismail, A.E.-A.S. Fouda, E.A. Ghaith, A fruitful century for the scalable synthesis and reactions of biphenyl derivatives: applications and biological aspects, RSC advances 13 (27) (2023) 18262–18305.

[44] X. Wang, H.-Y. Fu, W. He, Y.-T. Xiang, Z.-C. Yang, Y. Kuang, S.-X. Yang, Synthesis and antibacterial activity evaluation of biphenyl and dibenzofuran derivatives as potential antimicrobial agents against antibiotic-resistant bacteria, Curr. Issues Mol. Biol. 44 (9) (2022) 4087–4099.

[45] X. Li, J. Gao, C. Wu, C. Wang, R. Zhang, J. He, Z.J. Xia, N. Joshi, J.M. Karp, R. Kuai, Precise modulation and use of reactive oxygen species for immunotherapy, Sci. Adv. 10 (20) (2024) eadl0479.

[46] Q. Wang, M. Wang, Y. Chen, Q. Miao, W. Jin, Y. Ma, J. Pan, B. Hu, Deciphering microbiome and fungi–bacteria interactions in chronic wound infections using metagenomic sequencing, Eur. J. Clin. Microbiol. Infect. Dis. 43 (12) (2024) 2383–2396.

[47] C.B. Costa-Orlandi, J.C. Sardi, N.S. Pitangui, H.C. De Oliveira, L. Scorzoni, M. C. Galeane, K.P. Medina-Alarcón, W.C. Melo, M.Y. Marcelino, J.D. Braz, Fungal biofilms and polymicrobial diseases, Journal of Fungi 3 (2) (2017) 22.

[48] B.M. Peters, M.A. Jabra-Rizk, M.A. Scheper, J.G. Leid, J.W. Costerton, M. E. Shirtliff, Microbial interactions and differential protein expression in Staphylococcus aureus–Candida albicans dual-species biofilms, FEMS Immunol. Med. Microbiol. 59 (3) (2010) 493–503.
[49] L.M. Schlecht, B.M. Peters, B.P. Krom, J.A. Freiberg, G.M. Hänsch, S.G. Filler, M. A. Jabra-Rizk, M.E. Shirtliff, Systemic Staphylococcus aureus infection mediated by Candida albicans hyphal invasion of mucosal tissue, Microbiology 161 (1) (2015) 168–181.
[50] D.R. Cranendonk, F. Hugenholtz, J.M. Prins, P.H. Savelkoul, A.E. Budding, W. J. Wiersinga, The skin microbiota in patients hospitalized for cellulitis and association with outcome, Clin. Infect. Dis. 68 (8) (2019) 1292–1299.
[51] J. Lu, X. Liu, X. Li, H. Li, L. Shi, X. Xia, B.-l. He, T.F. Meyer, X. Li, H. Sun, Copper regulates the host innate immune response against bacterial infection via activation of ALPK1 kinase, Proc. Natl. Acad. Sci. 121 (4) (2024) e2311630121.
[52] W. Diao, P. Li, X. Jiang, J. Zhou, S. Yang, Progress in copper-based materials for wound healing, Wound Repair Regen. 32 (3) (2024) 314–322.
[53] W. Qiao, K.H. Wong, J. Shen, W. Wang, J. Wu, J. Li, Z. Lin, Z. Chen, J. P. Matinlinna, Y. Zheng, TRPM7 kinase-mediated immunomodulation in macrophage plays a central role in magnesium ion-induced bone regeneration, Nat. Commun. 12 (1) (2021) 2885.
[54] J.A. Maybin, N. Hirani, H.N. Jabbour, H.O. Critchley, Novel roles for hypoxia and prostaglandin E2 in the regulation of IL-8 during endometrial repair, Am. J. Pathol. 178 (3) (2011) 1245–1256.
[55] N.H. Gopee, E. Winheim, B. Olabi, C. Admane, A.R. Foster, N. Huang, R.A. Botting, F. Torabi, D. Sumanaweera, A.P. Le, A prenatal skin atlas reveals immune regulation of human skin morphogenesis, Nature (2024) 1–11.
[56] L. Xie, Z. Shan, L. Zhang, X. He, M. Gui, Y. Zhang, J. Xue, C. Ye, Y. Zou, M. Su, Metal ion “Adjuvant”[Si— O4] tetrahedron addresses coagulation interruption and promotes Multi-tissue regeneration via smart ionic capturing and cell membrane transporting, Adv. Funct. Mater. 35 (10) (2025) 2416743.
[57] L. Díez-Tercero, L.M. Delgado, E. Bosch-Rué, R.A. Perez, Evaluation of the immunomodulatory effects of cobalt, copper and magnesium ions in a pro inflammatory environment, Sci. Rep. 11 (1) (2021) 11707.
[58] Y. Ao, Y. Guo, Y. Zhang, L. Xie, R. Xia, J. Xu, M. Shi, X. Gao, X. Yu, Z. Chen, Hypoxia-mimicking mediated macrophage-elimination of erythrocytes promotes bone regeneration via regulating integrin αvβ3/Fe2+-Glycolysis-Inflammation, Adv. Sci. 11 (45) (2024) 2403921.
[59] P. Ahangar, X.L. Strudwick, A.J. Cowin, Wound healing from an actin cytoskeletal perspective, Cold Spring Harbor Perspect. Biol. 14 (8) (2022) a041235.
[60] M.T. Abreu-Blanco, J.J. Watts, J.M. Verboon, S.M. Parkhurst, Cytoskeleton responses in wound repair, Cell. Mol. Life Sci. 69 (2012) 2469–2483.
[61] S. Li, X. Wang, Z. Yan, T. Wang, Z. Chen, H. Song, Y. Zheng, Microneedle patches with antimicrobial and immunomodulating properties for infected wound healing, Adv. Sci. 10 (22) (2023) 2300576.
[62] L.D. Halder, S. Babych, D.I. Palme, E. Mansouri-Ghahnavieh, L. Ivanov, V. Ashonibare, D. Langenhorst, B. Prusty, G. Rambach, M. Wich, Candida albicans induces cross-kingdom miRNA trafficking in human monocytes to promote fungal growth, mBio 13 (1) (2022) e03563, 21.
[63] D. Kim, A. Sengupta, T.H. Niepa, B.-H. Lee, A. Weljie, V.S. Freitas-Blanco, R. M. Murata, K.J. Stebe, D. Lee, H. Koo, Candida albicans stimulates Streptococcus mutans microcolony development via cross-kingdom biofilm-derived metabolites, Sci. Rep. 7 (1) (2017) 41332.
[64] Y. Guo, S. Ding, C. Shang, C. Zhang, M. Li, Q. Zhang, L. Gu, B.C. Heng, S. Zhang, F. Mei, Multifunctional PtCuTe nanosheets with strong ROS scavenging and ROS-independent antibacterial properties promote diabetic wound healing, Adv. Mater. 36 (8) (2024) 2306292.
[65] C. Zhou, Z. Cai, J. Guo, C. Li, C. Qin, J. Yan, D. Yang, Injective hydrogel loaded with liposomes-encapsulated MY-1 promotes wound healing and increases tensile strength by accelerating fibroblast migration via the PI3K/AKT-Rac1 signaling pathway, J. Nanobiotechnol. 22 (1) (2024) 396.
[66] M.A. Pfaller, D. Diekema, Epidemiology of invasive candidiasis: a persistent public health problem, Clin. Microbiol. Rev. 20 (1) (2007) 133–163.